

Activity-rotation in the dM4 star Gl 729.

A possible chromospheric cycle.

R.V. Ibañez Bustos^{1,2,* **}, A.P. Buccino^{1,3}, S. Messina⁴, A.F. Lanza⁴, and P.J.D.

Mauas^{1,3}

¹ Instituto de Astronomía y Física del Espacio (CONICET-UBA), C.C. 67 Sucursal 28, C1428EHA-Buenos Aires, Argentina.

² Departamento de Física. FI-Universidad de Buenos Aires, Buenos Aires, Argentina.

³ Departamento de Física. FCEyN-Universidad de Buenos Aires, Buenos Aires, Argentina.

⁴ INAF-Osservatorio Astrofisico di Catania, via S. Sofia 78, 95123, Catania, Italia.

ABSTRACT

Aims. Recently, new debates on the role of layers of strong shear have emerged in the stellar dynamo theory. Further information on the long-term magnetic activity of fully convective stars could help disentangle if their underlying dynamo could sustain activity cycles similar to the solar one.

Methods. We perform a thorough study of the short- and long-term magnetic activity of the young active dM4 star Gl 729. First, we analyze long-cadence *K2* photometry to characterize its transient events (e.g. flares) and global and surface differential rotation. Then, from the Mount Wilson *S*-indexes derived from CASLEO spectra and other public observations, we analyze its long-term activity between 1998 and 2020 with four different time-domain techniques to detect cyclic patterns. Finally, we explore the chromospheric activity at different heights with simultaneous measurements of the $H\alpha$ and the Na I D indexes, and we analyze their relations with the *S*-Index.

Results. We found that the cumulative flare frequency follows a power-law distribution with slope ~ -0.73 for the range 10^{32} to 10^{34} erg. We obtained $P_{rot} = (2.848 \pm 0.001)$ days, and we found no evidence of differential rotation. We also found that this young active star presents a long-term activity cycle of ~ 4 -year length, with a less significant evidence of a shorter cycle of

* Contact e-mail: ribanez@iafe.uba.ar

** Based on data obtained at Complejo Astronómico El Leoncito, operated under agreement between the Consejo Nacional de Investigaciones Científicas y Técnicas de la República Argentina and the National Universities of La Plata, Córdoba and San Juan.

0.8 year. It also shows a broad activity minimum between 1998 and 2004. We found correlation between the S index, on one hand, and the H α the Na I D indexes, on the other, although these last two indexes reach a saturation level which is not observed in the Ca lines.

Conclusions. Since the maximum-entropy spot model does not reflect migration between active longitudes, this activity cycle could not be explained by a solar-type dynamo, and it is probably caused by an α^2 -dynamo.

Key words. stars: activity – stars: late-type – techniques: spectroscopic

1. Introduction

M dwarfs, with masses between 0.1 and 0.5 M_{\odot} , constitute a $\sim 75\%$ of the stars in the solar neighborhood. Approximately half of them show high chromospheric activity, larger than the solar one. They are usually referred to as dMe stars, because they have H α in emission, or flare stars, since they show frequent highly energetic flares (e.g. Günther et al. 2020; Rodríguez Martínez et al. 2020). The fraction of these active stars depends markedly on the spectral class (West et al. 2004, 2011; Reiners et al. 2012).

Stellar activity is supposedly driven by a stellar dynamo. In particular, for solar activity is the $\alpha\Omega$ dynamo, which is explained by the feedback between the differential rotation of the star, which stretches the lines of the poloidal magnetic field to produce a toroidal field (the Ω -effect), and the turbulent helical movements of the plasma in the convective zone, which regenerates the poloidal field (the α -effect, see Charbonneau (2010) for more details of the Solar dynamo process). In several dynamo models (e.g. Charbonneau & MacGregor 1997; Dikpati et al. 2005), the tachocline, an interface between the rigidly-rotating radiative core and the convection zone, plays a fundamental role. A solar-type dynamo can also successfully reproduce stellar activity cycles in cooler stars (e.g. Buccino et al. 2020).

However, dM stars with masses lower than $\sim 0.35 M_{\odot}$ are thought to be fully convective (Chabrier & Baraffe 1997) and, therefore, should not have a tachocline. Despite this fundamental difference in stellar structure, strong magnetic activity is also observed in very low-mass fully convective stars (Mauas & Falchi 1996; Hawley et al. 1996; West et al. 2004). Furthermore, stellar activity cycles were also detected in these stars (Cincunegui et al. 2007a; Díaz et al. 2007b; Suárez Mascareño et al. 2016; Wargelin et al. 2017; Ibañez Bustos et al. 2019b). Recently a new debate on the role of layers of strong shear was initiated by Wright & Drake (2016). They suggest that the presence of a tachocline should not be a critical ingredient in a solar-type dynamo. In this sense, Yadav et al. (2016) developed a dynamo model for the fully-convective star Proxima Centauri and concluded that large Rossby numbers (the ratio of stellar rotation period to convective turnover time) may promote regular activity cycles in fully-convective stars. Therefore, observational evidence of cyclic activity near the convection threshold and beyond can bring new contributions to this discussion (Buccino et al. 2014; Ibañez Bustos et al. 2019b; Toledo-Adrón et al. 2019).

The relationship between stellar rotation and magnetic activity is another fundamental key to understand the stellar dynamo. It shows an increase in activity when the rotation period decreases, with a saturated activity regime for fast-rotators. This relation was widely studied in different works using different indicators: by Wright et al. (2011), Wright & Drake (2016) and Wright et al. (2018) in X-ray emission (using L_X/L_{bol}), and by Astudillo-Defru et al. (2017) and Newton et al. (2017) in the optical range, **employing the $\log(R'_{HK})$ and $L_{H\alpha}/L_{bol}$, respectively.** In both the optical and X-ray ranges, these studies concluded that the transition in the inner structure of the stars does not imply a change in the dynamo mechanism (e.g. Wright & Drake 2016) and, therefore, stellar rotation plays an important role driving activity also in fully convective stars (e.g. Ibañez Bustos et al. 2019b). But even in that case, Astudillo-Defru et al. (2017) found three stars which do not belong to any of both regimes.

In this work we study in detail Gliese 729, which is one of the outliers in the saturation regime reported by Astudillo-Defru et al. (2017) **as its $\log(R'_{HK})$ value deviates more than 3σ from the fit (see Fig. 6 in Astudillo-Defru et al.).** We present a short and long-term activity analysis of this star using high precision photometry and a long series of spectroscopic observations. In section §2 we describe some features that make Gl 729 a specially interesting target. In section §3 we provide an overview of our optical spectroscopic observations together with the archival data also employed for the analysis. In sections §4 and §5, we present a detailed analysis of the photometric and spectroscopic data with different time-domain techniques and we explore the relation between different spectral features at different levels of activity. Finally, in section §6 we discuss the main conclusions of this analysis.

2. The target

Gl 729 (Ross 154, HIP 92403, V* V1216 Sgr) is an M4 active dwarf of the southern constellation of Sagittarius ($\alpha_{2000}=18^{\text{h}}549^{\text{m}}49.4^{\text{s}}$, $\delta_{2000}=-23^{\circ}50'10''$). This single star is the seventh M dwarf closest to our Sun with a distance of 2.97 pc, a radius of $0.19 R_{\odot}$ and a mass of $0.14 M_{\odot}$ (Gaidos et al. 2014).

Gl 729 is a flare star which has been observed in the optical (Falchi et al. 1990; Astudillo-Defru et al. 2017), X-ray (Wargelin et al. 2008; Malo et al. 2014) and EUV ranges (Tsikoudi & Kellett 1997). First, Kiraga & Stepien (2007) reported a rotation period of $P_{rot} = 2.869$ d for Gl 729 using ASAS photometry, confirmed by Díez Alonso et al. (2019). Considering this period and its coronal activity level, given by $\log(L_X/L_{bol}) = -3.5$ (Johns-Krull & Valenti 1996), Gl 729 is below the saturation regime ($L_X/L_{bol} = 10^{-3}$) reported by Wright et al. (2011).

Wargelin et al. (2008) studied the coronal magnetic activity using two Chandra observations. One of them presents a very large flare with evidence for the Neupert effect. And the other has several moderate flares. They found that the distribution of flare intensities does not appear to follow a single power law as in the solar case. They analyzed the non-flaring phase to search low level flaring, and they found that the microflaring explains the emission in this “quiescent” regime.

They found that the normalized X-ray luminosity L_X/L_{bol} is below 10^{-3} , which is near the mean value of the saturation regime.

Due to their low masses, M dwarf stars are also ideal targets to detect terrestrial planets from ground (e.g. Anglada-Escudé et al. 2016; Ribas et al. 2018; Díaz et al. 2019) or from space (e.g. Muirhead et al. 2012; Winters et al. 2019). Furthermore, statistical studies show a high occurrence of small planets around M stars (Bonfils et al. 2013; Dressing & Charbonneau 2015). However, activity features could hide an exoplanet signal and even mimic it (Robertson & Mahadevan 2014). Therefore, great efforts have been developed to disentangle activity and planetary signals in the RV-series (e.g. Desort et al. 2007; Haywood et al. 2014; Díaz et al. 2016) or transiting curves (e.g. Boisse et al. 2012; Bonomo & Lanza 2012; Aigrain et al. 2016; Morris et al. 2020). For this reason, an exhaustive characterization of the stellar magnetic activity over different time scales could allow to detect extrasolar planets even around active stars. In particular, Gl 729 belongs to the CARMENES input catalog (Reiners et al. 2018), which is not biased by activity level. Although Gl 729 has been observed by different programs, it has not been studied in the optical range in detail. Here, we present an extensive study of this dMe variable star based on around twenty years of spectroscopic observations.

3. Observations

The HK α Project was started in 1999 with the aim to study long-term chromospheric activity of southern cool stars. In this program, we systematically observe late-type stars from dF5 to dM5.5 with the 2.15 m Jorge Sahade telescope at the CASLEO observatory which is located at 2552 m above sea level, in the Argentinian Andes. The medium-resolution echelle spectra ($R \approx 13.000$) were obtained with the REOSC¹ spectrograph. They cover a maximum wavelength range between 3860 and 6690 Å. We calibrate all our echelle spectra in flux using IRAF² routines and following the procedure described in Cincunegui & Mauas (2004). In this work, we employed 19 observations distributed between 2005 and 2019. Each observation consists of two consecutive spectra with 45 minutes exposure time each, which are combined to eliminate cosmic rays and to reduce noise.

We complemented our data with public observations obtained with several spectrographs, by the programs listed in Table 2. Sixty echelle spectra were observed by HARPS, mounted at the 3.6 m telescope ($R \sim 115.000$) at La Silla Observatory (LSO, Chile), distributed over the year 2005 and the interval 2015 – 2017. Only one FEROS spectrum was available in our study. This spectrograph is placed on the 2.2 m telescope in LSO and has a resolution of $R \sim 48.000$. Four spectra were taken in the years 2011 and 2015 with UVES, attached to the Unit Telescope 2 (UT2) of the Very Large Telescope (VLT) ($R \sim 80.000$) at Paranal Observatory. Two mid-resolution spectra ($R \sim 8.900$) in the UVB wavelength range (300 - 559.5 nm) were obtained in 2014 with the X-SHOOTER

¹ <http://www.casleo.gov.ar/instrumental/js-reosc.php>

² The Image Reduction and Analysis Facility (IRAF) is distributed by the Association of Universities for Research in Astronomy (AURA), Inc., under contract to the National Science Foundation

spectrograph, mounted at the UT2 Cassegrain focus also at VLT. Finally, we employed 13 spectra from the HIRES spectrograph mounted at the Keck-I telescope distributed along 1998 and 2010.

HARPS and FEROS spectra have been automatically processed by their respective pipelines^{3,4}, while UVES and XSHOOTER observations were manually calibrated with the corresponding procedure.^{5,6}

In this work, we also analyzed high precision photometry obtained during the *K2* mission by the *Kepler* spacecraft (Borucki et al. 2010). *K2* observed a total of 20 fields in sequential series of observational campaigns lasting ~ 80 d each. Throughout the mission, *K2* observed in two cadence modes: short cadence (one observation every minute) and long cadence (one observation every ~ 30 minutes). In this study, we analyze the long-cadence observations of Gl 729 during the campaign 7 of the GO7016_GO7060 proposal, obtained between 2015 October, 4th and 2015 December, 26th.

4. Analysis of *K2* Photometry

In this section, we first present an analysis of the short-term activity of Gl 729, derived from the *Kepler* light curve. We also model the stellar variability with a maximum-entropy spot model to derive active longitudes and estimate a minimum amplitude for the stellar differential rotation.

4.1. Flare activity and Rotation

To study the magnetic variability of Gl 729, we employed high-quality photometry obtained by the *K2* mission. The *Kepler* database provides short- and long-cadence light curves, which constitute a great basis to detect flare-like events (e.g. Hawley et al. 2014; Davenport et al. 2016). Only long-cadence photometry is available for Gl 729.

In order to analyze both the rotational modulation and detect these transients events in the *Kepler* light curve, we analyzed the time series with the FLARE deTECTION With RANSAC Method (FLATW'RM) algorithm based on machine learning techniques (Vida & Roettenbacher 2018)⁷. In particular, the FLATW'RM code first determines the stellar rotation period and, after subtracting the fitted rotational modulation from the light curve, it detects the flare-like events and reports the starting and ending time, and when the maximum flux of the flare occurs.

In Fig. 1 we show the photometric time series for Gl 729, where an appreciable rotational modulation can be noted. The red points indicate the flares detected by FLATW'RM, for $N=2$ and a detection limit of 3σ . These parameters were selected according to the statistical characteristics of flares of active M stars. According to Günther et al. (2019), the equivalent duration of a flare in an active M0-M4 or M4.5-M10 star lies between ~ 1 and ~ 120 minutes. Therefore, given the 30-minute cadence of the *Kepler* light curve in Fig. 1, we requested at least 2 consecutive points above the detection-limit to consider a single flare lasting at least 30 minutes. Shorter flares could not be

³ <http://www.eso.org/sci/facilities/lasilla/instruments/harps.html>

⁴ <http://www.eso.org/sci/facilities/lasilla/instruments/feros.html>

⁵ <http://www.eso.org/sci/facilities/paranal/instruments/uves.html>

⁶ <http://www.eso.org/sci/facilities/paranal/instruments/xshooter.html>

⁷ FLATW'RM is available at <https://github.com/vidakris/flatwrm/>.

detected with this sampling. We found a total of 47 flare events along ~ 81 days. An estimation of the flare energy can be obtained by integrating the flare normalized intensity during the event between the beginning and the end times detected by the algorithm (see Vida & Roettenbacher 2018 for more details). This equivalent duration ε_f is multiplied by the quiescent stellar luminosity (F_\star), to obtain the energy in the observed passband (ξ_f). We estimated the quiescent luminosity integrating a flux calibrated X-SHOOTER spectrum of Gl 729, convolved with the *Kepler* response function, to obtain the observed quiescent luminosity in the *Kepler* pass band, and we obtain $F_\star = 1.3 \times 10^{30} \text{ erg s}^{-1}$.

Following the analysis of Gizis et al. (2017), we studied the cumulative flare frequency distribution ν , (i.e. the number of flares with a given energy or greater divided by the total time of observation in the light curve). It can be expressed as:

$$\log \nu = a + \beta \log \xi_f. \quad (1)$$

The slope $\beta = (1 - \alpha)$ is found fitting the distribution by a linear function, where α is used to characterize how the flare energy of the star is dissipated. In Fig. 2 we show the best linear fit for the energy range indicated with dashed black lines. We obtained a value of $\alpha = 1.71$ from this least minimum-squares fit. Gizis et al. (2017) proposed an alternative method to calculate α using a maximum likelihood estimator for the small sample size

$$(\alpha - 1) = (n - 2) \left[\sum_{i=1}^n \ln \frac{\xi_i}{\xi_{min}} \right]^{-1} \quad (2)$$

where n is the number of transient events and ξ_i and ξ_{min} are the individual and lowest flare energies, respectively. With this method, we obtain $\alpha = 1.73$ which is consistent with the linear-fit value.

Thus, Gl 729 flares follow a power law slope $\beta \sim 0.71$ between 10^{32} and 10^{34} erg. Considering that the energy flux in the quiescent state is around $10^{30} \text{ erg s}^{-1}$, the energy release during a flare event is larger by 2 to 4 orders of magnitude than the time-integrated stellar luminosity.

To analyze the rotational modulation we discarded the flares detected by FLATW'RM. We studied the resulting light curve, shown in Fig. 3, using the Generalized Lomb-Scargle (GLS) periodogram (Zechmeister & Kürster 2009) in Fig. 4. The most significant period we detected is the rotation period found in the literature (see Section 2). We obtained $P_{rot} = (2.848 \pm 0.001)$ days with a high significance (FAP < 0.1 %). We also found a second peak of $P = (1.427 \pm 0.001)$ days, half P_{rot} , with lower significance. Following Lamm et al. (2004), we estimate the error of the detected period as $\delta P = \frac{\delta \nu P^2}{2}$, where $\delta \nu$ is the finite frequency resolution of the periodogram. In Fig. 3, we also plot the best fit with two harmonic functions of these two periods with a red line.

This bimodality could be associated to two dominant spots in opposite hemispheres, with areas A_1 and $A_2 < A_1$. This case would be equivalent to having a "symmetric" spot with area A_2 , in both

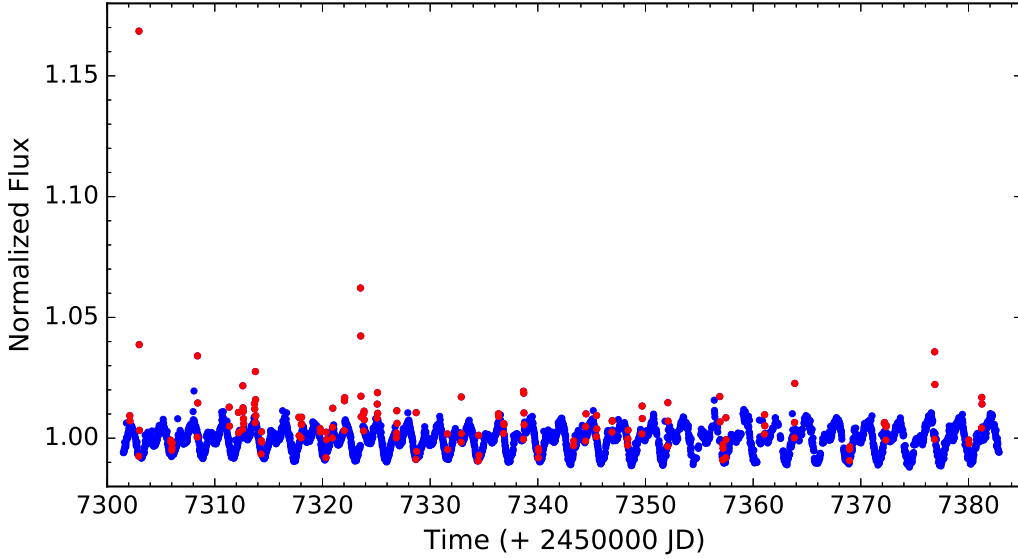


Fig. 1. Long-cadence *K2* photometric light-curve for Gl 729. Selected flare candidates are shown with red points.

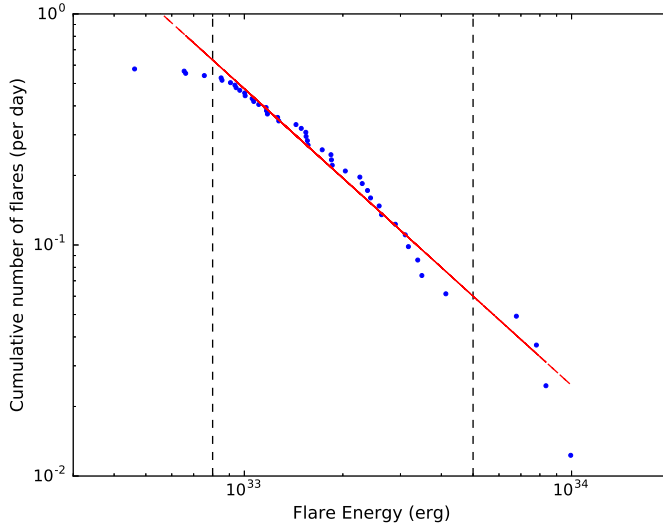


Fig. 2. Gl 729. Cumulative frequency of flares ν derived from the *Kepler* light curve with the FLATWR'M algorithm. The red solid line is the best linear fit (Eq. 1) in the range 8×10^{32} - 5×10^{33} erg with $\alpha = 1.71$

hemispheres, rotating with $P_{rot}/2$ and an "asymmetric" spot with area $A_1 - A_2$, only in one hemisphere, rotating with P_{rot} . McQuillan et al. (2013) performed a statistical analysis of *Kepler* light curves of a series of M stars, and found that several stars of their sample present this bimodality in their rotation periods.

4.2. Spot modelling

A critical ingredient of the $\alpha\Omega$ dynamo is the differential rotation in the stellar interior (e.g. convection zone). A good proxy could be its surface differential rotation (see e.g. Buccino et al. 2020), which could be derived from the stellar-spots migration.

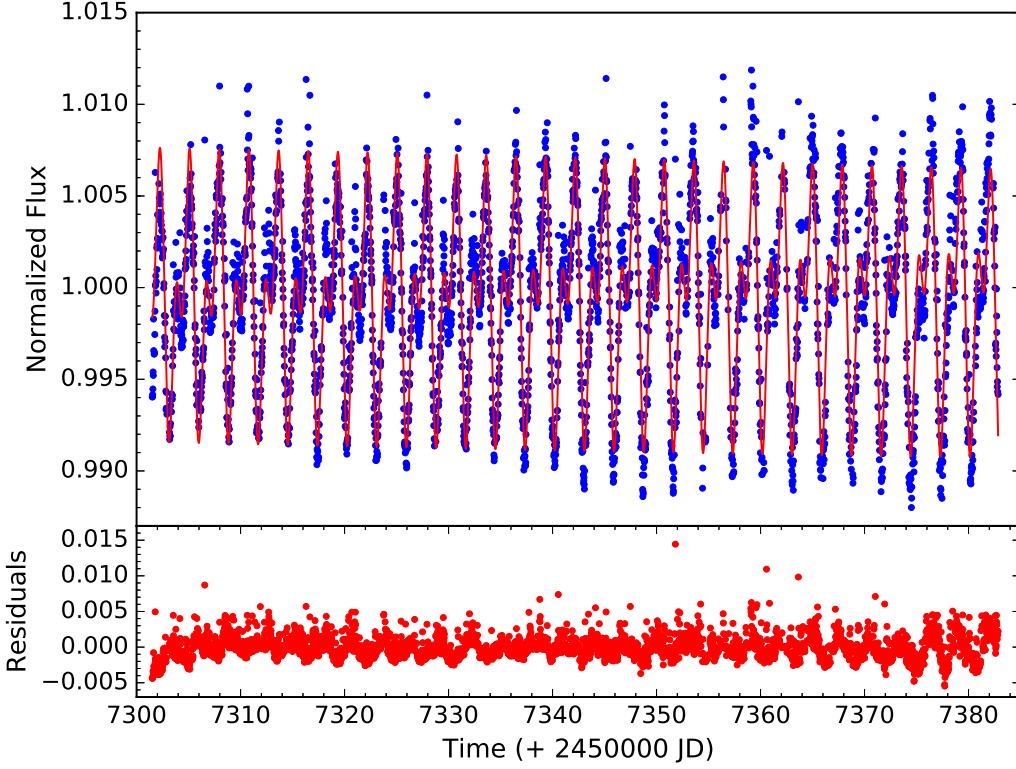


Fig. 3. *K2* long-cadence photometry for Gl 729 without the flare candidates detected with the FLATW'RM algorithm. The red solid line represents the least-square fit with two harmonic function of the periods found with the GLS periodogram (2.848 days and 1.427 days).

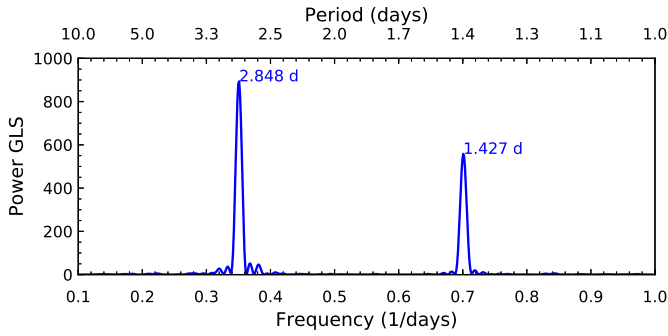


Fig. 4. GLS periodogram for the non-flaring *K2* light curve of Fig. 3.

When the light curve is phased with the average rotation period, the mean longitude of the activity centers at latitudes with rotation either shorter or longer than the average one are expected to exhibit a migration. The spot modelling is one possible approach to infer such a migration.

In the present study, we applied a spot modelling approach which is the same already introduced in Bonomo & Lanza (2012) to which we refer the reader for details. In brief, the surface of the star is subdivided into 200 surface elements that contain unperturbed photosphere, dark spots, and solar-like faculae. The specific intensity of the unperturbed photosphere in the *Kepler* passband is assumed to vary according to a quadratic limb-darkening law:

$$I(\mu) = I_0(a_p + b_p\mu + c_p\mu^2), \quad (3)$$

where I_0 is the specific intensity at the centre of the disc, $\mu = \cos \theta$ with θ being the angle between the local surface normal and the line of sight, and a_p , b_p , and c_p are the limb-darkening coefficients in the *Kepler* passband (Claret & Bloemen 2011).

The dark spots are assumed to have a fixed contrast $c_s \equiv I_{\text{spot}}(\mu)/I(\mu)$ in the *Kepler* passband, where I_{spot} is the specific intensity in the spotted photosphere. The fraction of a surface element covered by dark spots is given by its filling factor f .

This model is fitted to a segment of the light curve of duration Δt_f (see Sect. 4.3) by varying the filling factors of the individual surface elements that can be represented as a 200-element vector \mathbf{f} . The spot pattern is assumed to stay fixed along each interval of duration Δt_f , which is a fundamental assumption of our modelling because a significant spot evolution occurring on a shorter timescale may hamper our approach.

Our model has 200 free parameters and suffers from non-uniqueness and instability due to the effect of photometric noise. To select a unique and stable solution, we apply a maximum entropy regularization by minimizing a functional Z that is a linear combination of the χ^2 and of a suitable entropy function E :

$$Z = \chi^2(\mathbf{f}) - \lambda E(\mathbf{f}), \quad (4)$$

where $\lambda > 0$ is a Lagrangian multiplier that controls the relative weights given to the χ^2 minimization and the configuration entropy of the surface map E in the solution. The expression of E is given in Eq. (4) of Lanza et al. (1998) and it is maximal when the star is unspotted, that is all the elements of the vector \mathbf{f} are zero. In other words, the maximum entropy (hereafter ME) criterion selects the solution with the minimum spotted area compatible with a given χ^2 value of the best fit to the light curve. When the Lagrangian multiplier $\lambda = 0$, we obtain the solution corresponding to the minimum χ^2 that is unstable. By increasing λ , we obtain a unique and stable solution at the price of increasing the value of the χ^2 . An additional effect is that of making the residuals between the model and the light curve biased towards negative values because we reduce the spot filling factors by introducing the entropy term (see Lanza (2016), for more details).

The information on the latitude of the spots is lacking in our maximum-entropy maps because the inclination of the stellar spin axis is very close to 90° (cf. Sect. 4.3) that makes the transit time of each feature independent of its latitude. Therefore, we shall limit ourselves to map the distribution of the filling factor versus the longitude.

The optimal value of the Lagrangian multiplier λ is obtained by imposing that the mean μ_{reg} of the residuals between the regularized model and the light curve verifies the relationship (Bonomo & Lanza 2012; Lanza 2016):

$$|\mu_{\text{reg}}| = \frac{\sigma_0}{\sqrt{N}}, \quad (5)$$

where σ_0 is the standard deviation of the residuals of the unregularized model, that is that computed with $\lambda = 0$, and N the number of datapoints in the fitted light curve interval of duration Δt_f .

The optimal value of Δt_f is not known a priori and must be determined with an analysis of the light curve itself because it is related to the lifetimes of the active regions in a given star. We shall adopt a unique value of Δt_f for the entire light curve of Gl 729 because the ratio $\Delta t_f/P_{\text{rot}}$, where P_{rot} is the stellar rotation period, rules the sensitivity of the spot modelling to active regions located at different longitudes as discussed by Lanza et al. (2007).

The optimal value of the facular-to-spotted area ratio Q could also be derived from the light curve best fit. Considering that at the young age of Gl 729 the activity is dominated by dark spots, and considering that for any value of Q , we found highly structured maps that barely represent the double-dip shape of the light curve, we decided to fix $Q = 0$, that is we included only dark spots in our model.

4.3. Stellar parameters

The basic stellar parameters, that is mass, radius and effective temperature T_{eff} are taken from references in Table 1. They do not directly enter into our geometric spot model, except for the computation of the relative difference ϵ_{rot} between the polar and the equatorial axes of the ellipsoid used to represent the surface of the star. Their values are obtained by a simple Roche model assuming rigid rotation with a period of $P_{\text{rot}} = 2.848$ days. The gravity darkening effect associated with $\epsilon_{\text{rot}} \sim 4.1 \times 10^{-5}$ is much smaller than the photometric precision, thus it can be neglected in our model. The inclination of the stellar rotation axis is assumed to be $i = 90^\circ$ because a star viewed equator-on is compatible with the stellar radius, the rotation period and the projected rotational velocity *v.sini*.

The contrast of the dark spots $c_s = 0.90$ was inferred from the work of Andersen & Korhonen (2015). The duration of the individual segments of the light curves has been kept at $\Delta t_f = 2.848$ days, that is the rotation period. We found that increasing Δt_f makes the total χ^2 worse. On the contrary, keeping $\Delta t_f = 2.848$ days we get a better time resolution in the description of the spot evolution, since the active region growth and decay in Gl 729 has a time scale comparable or longer than the rotation period. Choosing Δt_f equal to the rotation period is also optimal because it grants a uniform sampling of all the longitudes by our spot modelling (Lanza et al. 2007).

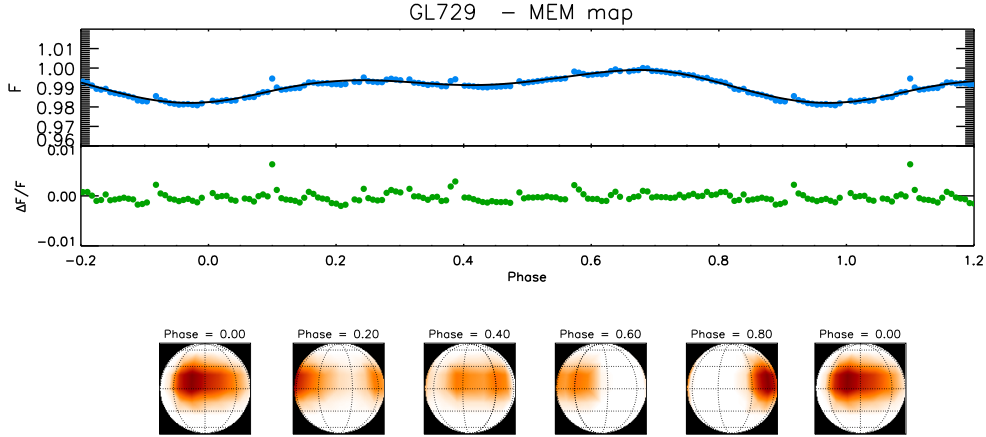
To infer information on the age, we checked possible membership with known associations or moving groups using the BANYAN Σ tool (Gagné et al. 2018). We found 99.9% probability Gl 729 is a field star. Using relations between age, rotation period, and X-ray luminosity ($\log L_X = 27.05$; Wright et al. 2011) calibrated for M2-M6 stars (Engle & Guinan 2018; 2011) we infer an age in the range from 0.2 Gyr to 0.6 Gyr. This result is supported by the relatively high rotation velocity ($v \sin i = 3.5 \pm 0.5 \text{ km s}^{-1}$) reported by Johns-Krull & Valenti 1996), which indicates that Gl 729 is a young star with an estimated age of less than 1 Gyr.

Table 1. Parameters adopted for the modelling of the light curves of Gl 729.

Parameter	Value	Ref.
Star mass (M_{\odot})	0.14	Gaidos et al. (2014)
Star radius (R_{\odot})	0.19	Gaidos et al. (2014)
T_{eff} (K)	3213	Gaidos et al. (2014)
$v \sin i$ (km s^{-1})	3.5 ± 0.5	Johns-Krull & Valenti (1996)
a_p	0.2023	Claret & Bloemen (2011)
b_p	1.1507	Claret & Bloemen (2011)
c_p	-0.3530	Claret & Bloemen (2011)
P_{rot} (days)	2.848	present study
ϵ_{rot}	4.1×10^{-5}	present study
i (deg)	90.0	present study
c_s	0.90	Andersen & Korhonen (2015)
Q	0.0	present study
Δt_f (days)	2.848	present study

4.4. Model results

As mentioned in Sect. 4.2, we found the standard deviation σ_0 of the residuals of the unregularized model (obtained by imposing $\lambda = 0$) to be $\sim 1.1 \times 10^{-3}$ and the average number of datapoints in the fitted light curve interval of duration Δt_f to be $N \simeq 110$. After a number of trials, we found Eq. (4) to be satisfied with $|\mu_{\text{reg}}| \sim 1.0 \times 10^{-4}$. In Fig. 5, we show an example of the results of our spot modelling for the epochs from BJD 2457340.26 until 2457343.11 spanning a single star’s rotation.


Fig. 5. Example of spot modelling of a single star’s rotation.

In the top panel we show the normalized flux with the best fit over plotted, in the middle panel the distribution of residuals, and finally, in the bottom panel the spot maps at five selected rotation phases. The presence of two major spot groups of different sizes on opposite hemispheres is evident, which is compatible with the discussion in Sect. 4.1. We note that the *Kepler K2* PDCSAP fluxes used in the present analysis show evidence of residual instrumental effects, which are better

evident in the residual plot as discontinuities about every 0.1 intervals in rotation phase. However, the computed model (solid line) is apparently unaffected by this issue.

As anticipated, we are specifically interested to check possible migration of the longitude at which spots are located. This is accomplished in Fig. 6, where we plot the distribution of the filling factor of the starspots f versus the longitude and the time for the regularized spot maps. The origin of the longitude is at the meridian pointing toward the Earth on BJD 2457303.243 and the longitude is increasing in the same direction as the stellar rotation. We identify two activity centers, a dominant one located at about longitude zero and another of smaller size on the opposite hemisphere. These centers could be associated to the two peaks observed in the GLS periodogram of Fig. 3, one corresponding to the rotation period and the other to its first harmonic. We note some hint for an oscillation in the longitude of the dominant center of activity. However the amplitude of such a migration, which is of the order of about 50° is comparable or smaller than the longitude resolution achieved by our spot modelling.

Our spot modelling allows us to determine the variation of the total spotted area vs. the time by integrating the filling factor over the longitude. The error is estimated from the photometric accuracy of the datapoints. The presence of gaps inside each individually-fitted interval of duration Δt_i affects the total area because the maximum entropy regularization drives the solution towards the minimum spotted area compatible with the data, thus reducing the filling factor at the longitudes that are in view during the gaps in the light curves.

To reduce the impact of this effect on the variation of the total spotted area, we measured the presence of significant gaps along each interval Δt_i . We divided each interval into five equal subintervals and counted the number of datapoints into each subinterval n_i , with $i = 1, \dots, 5$ numbering the subinterval. A measure δ of the inhomogeneous distribution of the datapoints along the interval Δt_i is defined as $\delta \equiv [\max(n_i) - \min(n_i)] / \max(n_i)$. The intervals with $\delta > 0.2$ are discarded giving a total of 21 area measurements unaffected by the gaps over a total of 27 intervals.

The plot of the total spotted area vs. the time for this light curve is shown in Fig. 7. The duration of the time interval is too short to conclude about the cause of the area variation that could be associated with the growth and decay of the individual active regions in the active longitudes.

5. Chromospheric activity

In this section we present an analysis of the long-term activity of the flare active M4 dwarf, Gl 729. We present a magnetic activity analysis by compiling our own and public spectroscopic data building a registry of activity which allows us to detect cyclic patterns.

5.1. Mount Wilson S -Index

Stellar activity cycles have been detected in several late-type stars, typically measuring fluctuations in the well-known dimensionless Mount Wilson S -Index (e.g. Baliunas et al. 1995; Metcalfe et al. 2013; Ibañez Bustos et al. 2019a). This activity indicator S is defined as the ratio between the

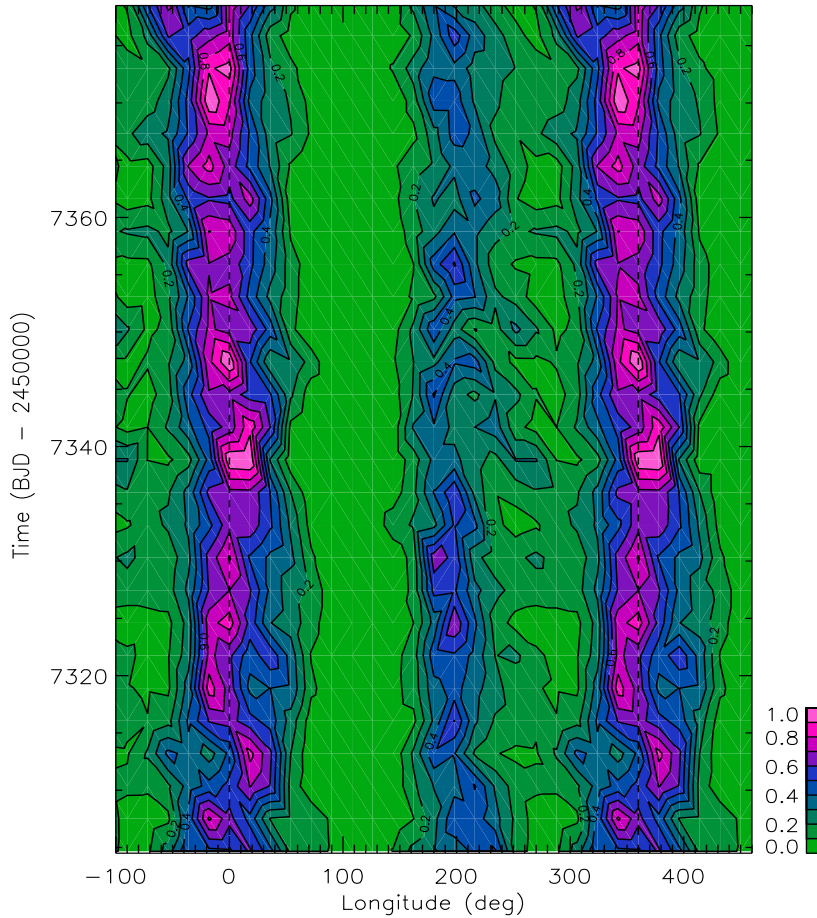


Fig. 6. Distribution of the spot filling factor vs. the longitude and time as derived by our maximum-entropy spot model. The maximum of the filling factor is indicated by the purple colour, while the minimum by green (see colour scale in the lower right corner). We note that the longitude scale is repeated beyond the $[0^\circ, 360^\circ]$ interval.

chromospheric Ca II H and K line-core emissions, integrated with a triangular profile of 1.09 \AA FWHM, and the photospheric continuum fluxes integrated in two 20 \AA passband centred at 3891 and 4001 \AA (Duncan et al. 1991). For decades, the S -Index was mainly used to study the chromospheric activity only for dF to dK stars (Baliunas et al. 1995), as larger exposure times are needed to observe the Ca II lines in later stars, which are both redder and fainter. Later, Cincunegui et al. (2007b) studied the usefulness of the S index, and other activity indicators, for dM stars.

To search for indications of stellar activity in Gl 729 we computed the S -index for the spectra mentioned in Sect. 3. For our CASLEO observations, we used the method described in Cincunegui et al. (2007b). For the other spectra, we followed Duncan et al. (1991). We then calibrated the HARPS indexes to the Mount Wilson S -index with the calibration available in Lovis et al. (2011),

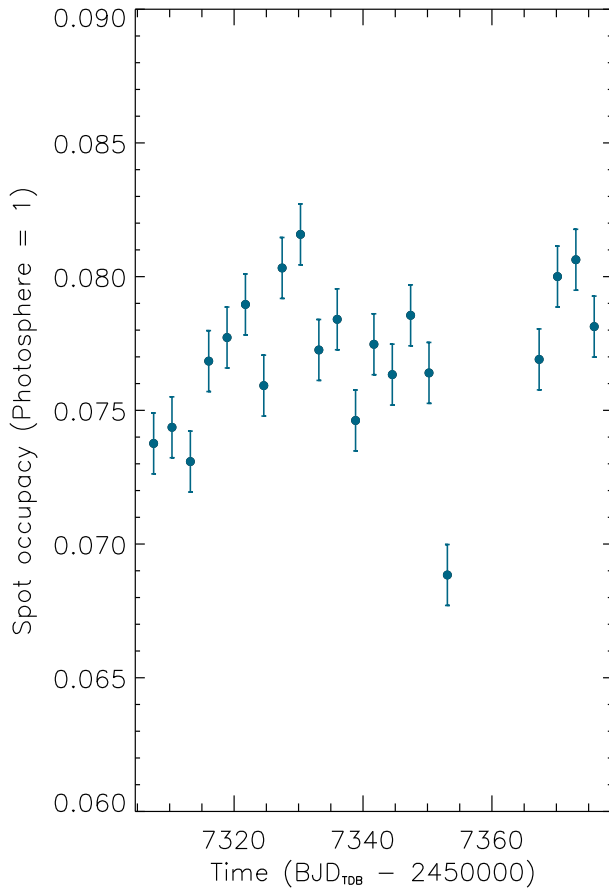


Fig. 7. The total spotted area as derived from the ME best fits to the light curve vs. the time. The error bars have an amplitude of 3σ , where σ is the standard deviation as derived from the photometric accuracy of the datapoints.

and the FEROS spectra with the procedure used in Jenkins et al. (2008). Finally, as we have done in previous work (Ibañez Bustos et al. 2019a,b), we intercalibrated the CASLEO, FEROS, UVES, XSHOOTER and HIRES indexes considering as reference the calibrated HARPS Mount Wilson indexes closest in time. Our time series is composed by 99 measurements for a time span between 1998 and 2019. These data is shown in Fig. 8 and listed in Table 2.

We estimated a 4% typical error of the S -Index derived from CASLEO (see deduction in Ibañez Bustos et al. 2019a). The error bars of the S -indexes derived from HARPS, FEROS, UVES, XSHOOTER and HIRES spectra were calculated as the standard deviation of each monthly bin. The rotational modulation in the S index may contribute to its daily variation, we estimated it $\sim 15\%$ from HARPS observations. For time intervals with only one ESO observation in a month, we adopted the typical RMS dispersion of the bins. The whole time series presents a variability of $\sigma_S/\langle S \rangle \sim 27\%$ along 21 years.

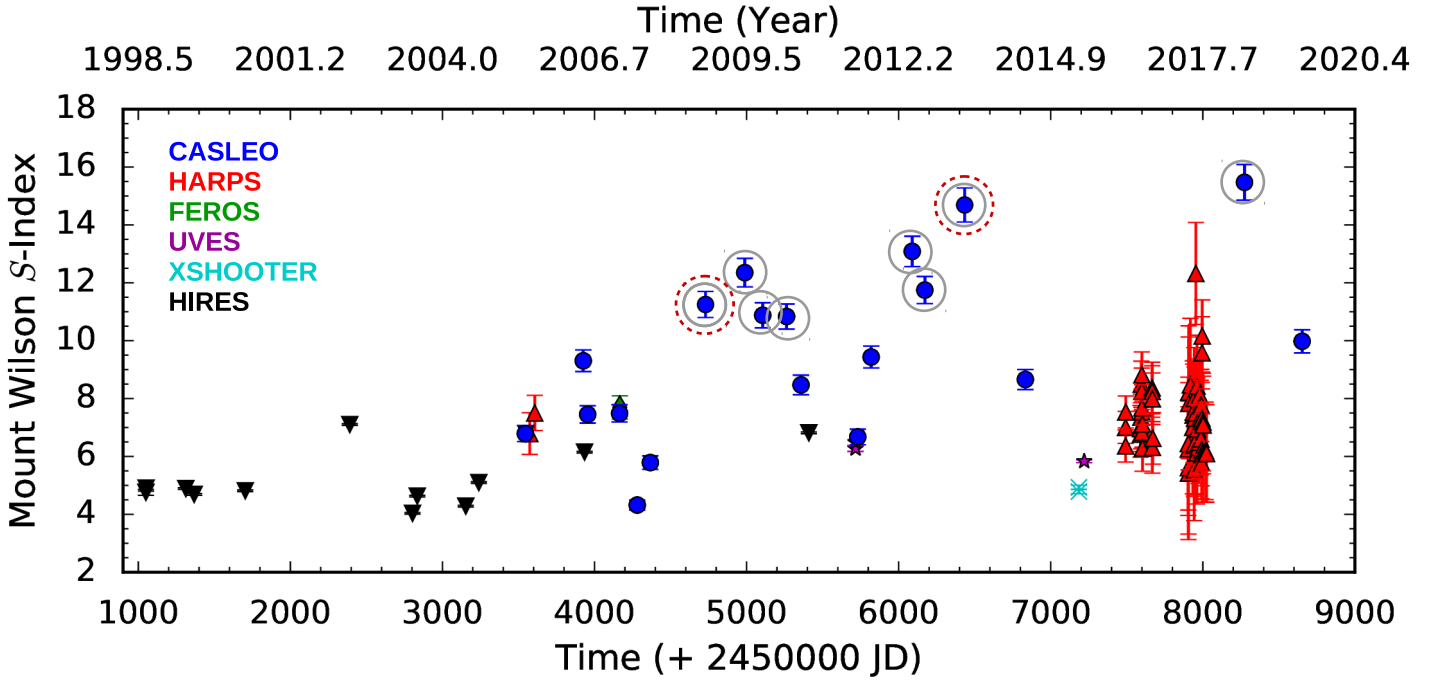


Fig. 8. Mount Wilson S -indexes for Gl 729 derived from CASLEO (blue circles), HARPS (red triangles), FEROS (green diamonds), UVES (magenta stars), XSHOOTER (cyan cross) and HIRES (black inverted triangles) spectra. We highlight with gray circles the CASLEO spectra where an increase in activity is observed. In red dashed circles we show the two observations we discarded from our analysis.

5.2. Long-term variations

The time series plotted in Fig. 8 shows a near flat regime between the years 1998 and 2004, and then an increasing trend until the maximum in 2018 ($xJD = 8300$ days). First, we analyzed if this growth is due to the gradual increase of the mean magnetic activity or to particular observations of transient high-energy phenomena (e.g. flares). Gl 729 has a flare frequency of 0.5 flares per day of at least 10^{33} erg (see Fig. 2). To filter out these events, we visually compared the individual spectra that form each of our observations (see Section §3), for the dates marked with gray circles in Fig. 8.

In Fig. 9 we show the individual line profiles of the Ca II K line for these observations. We show in red the first observation and in green the second one. It can be seen that there is a difference of 85% between the two spectra taken in September, 2008 (0908), and a difference of 78% between those taken in May, 2013 (0513). We excluded these two observations from our analysis, since they were probably obtained during flares. For the observation taken in June 2018 (0618) we see a difference of almost 38% between individual spectra. In this case we decided to include only the first observation (red line in Fig. 9) since it shows a line flux similar to the rest of the non-flaring observations. For the other observations the difference between both fluxes is from 6 to 11%, consistent with the calibration error (Cincunegui & Mauas 2004).

From the remaining data, we obtained a mean Mount Wilson index $\langle S \rangle = 7.343 \pm 1.967$ and a Ca II emission level of $\log R'_{HK} = -4.645$, both in agreement with the values reported by Astudillo-Defru et al. (2017). Considering the rotation period for Gl 729 of 2.848 days, the $\log R'_{HK}$ confirms

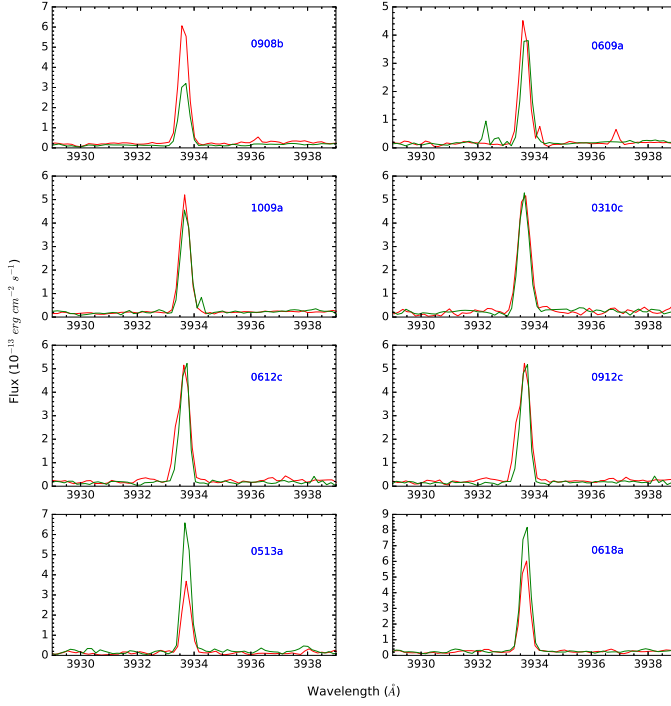


Fig. 9. Ca II K line for CASLEO individual observations. Each plot is labeled with the date of each observation (MMYY). We plot in red the first observation and in green the second consecutive one at the same night.

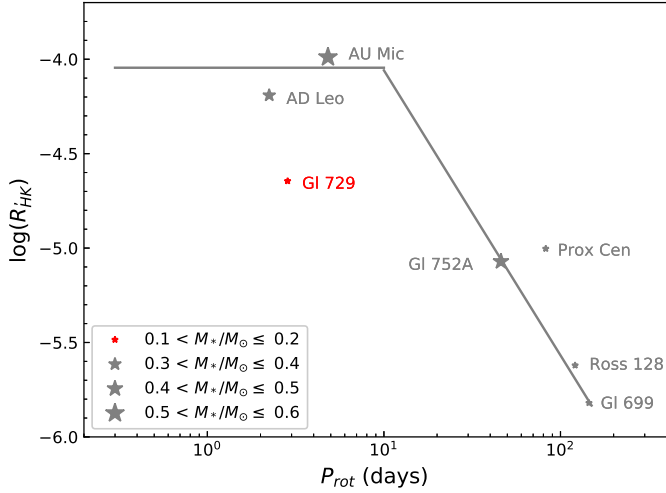


Fig. 10. $\log R'_{HK} - P_{rot}$ diagram including the Astudillo-Defru et al.'s fit (gray solid lines). With gray stars we show five M dwarfs with activity cycles detected using CASLEO spectra (Prox Cen: Cincunegui et al. (2007a); Gl 752A: Buccino et al. (2011); AD Leo: Buccino et al. (2014); AU Mic: Ibañez Bustos et al. (2019a) and Ross 128: Ibañez Bustos et al. (2019b)). The activity cycle of Gl 699 was detected by Toledo-Adrón et al. (2019) employing seven independent sets of spectroscopic observations. With a red star we represent Gl 729 which is a clear outlier from the saturated regime of this diagram.

that this star is an outlier in the saturation regime reported for dM stars in the $\log R'_{HK} - P_{rot}$ diagram (Astudillo-Defru et al. 2017). In Fig. 10 we plot the fit obtained by Astudillo-Defru et al. (2017) from the HARPS database. We also include five stars with magnetic activity cycles detected employing CASLEO spectra and Gl 699 (Barnard's star), whose activity cycle was reported by Toledo-Adrón et al. (2019) using a different set of spectroscopic data.

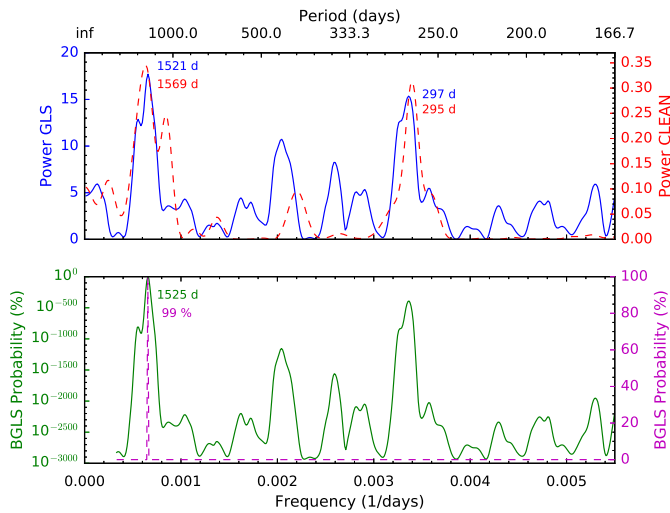


Fig. 11. *Top:* GLS (solid blue line) and CLEAN (dashed red line) periodograms for the *S* time series of Gl 729. The most prominent peaks for the GLS periodogram with a FAP < 0.1% are: (1521 ± 20) days and (297 ± 2) days. *Bottom:* Bayesian percentage probability indicates with the 99 % of probability that the ~ 1500 -day peak is the real activity cycle.

To search for long-term activity cycles in the remaining data series, we implement three different methodologies. In the top panel of Fig.11 we show the GLS periodogram together with the results of the CLEAN deconvolution algorithm developed by Roberts et al. (1987). Both analysis show a very significant peak at $P_1 = (1521 \pm 20)$ days for the GLS and a slightly larger value for the CLEAN periodogram, and a less significant one at $P_2 = (297 \pm 2)$ days, both with FAP < 0.1 %.

In Fig. 11 (bottom) we present the results of the Bayesian Generalized Lomb-Scargle periodogram described by Mortier et al. (2015) which expresses “the probability that a signal with a specific period is present in the data”. The green line indicates the logarithmic probability and the dashed magenta line, the linear probability. Thus, we conclude that both cycles are present in the data, although the ~ 1500 -days activity cycle, with a 99% probability, is markedly more significant than the one with $P = 296$ days.

Böhm-Vitense (2007) examined the relation between P_{rot} and P_{cyc} for a set of cyclic FGK stars, expanding the work done previously (Brandenburg et al. 1998; Saar & Brandenburg 1999). She found that most stars are well distributed in two branches in the $P_{cyc} - P_{rot}$ diagram (her Fig 2). A possible interpretation is that each sequence corresponds to a different type of dynamo. If we include our results in this $P_{cyc} - P_{rot}$ diagram, we find that the 1500-days cycle belongs to the active branch labeled as “Aa” in that figure. For the stars in this branch, the number of rotational revolutions per activity cycle is around $P_{cyc}/P_{rot} \sim 500$, which is consistent with the value of $1521/2.848 = 534$ we obtain for Gl 729. Similarly, the less significant activity cycle of $P_{cyc} \sim 300$ days detected lies within the inactive branch, where the ratio $P_{cyc}/P_{rot} \sim 90$. Furthermore, as we have show in §4.3, Gl 729 is a young star, which is coherent with the conclusion by Böhm-Vitense (2007), that stars which belong to the Aa-sequence are younger than the Sun. This suggests that Böhm-Vitense’s diagram could be extended to cyclic M stars. **In Fig. 12 we show the updated**

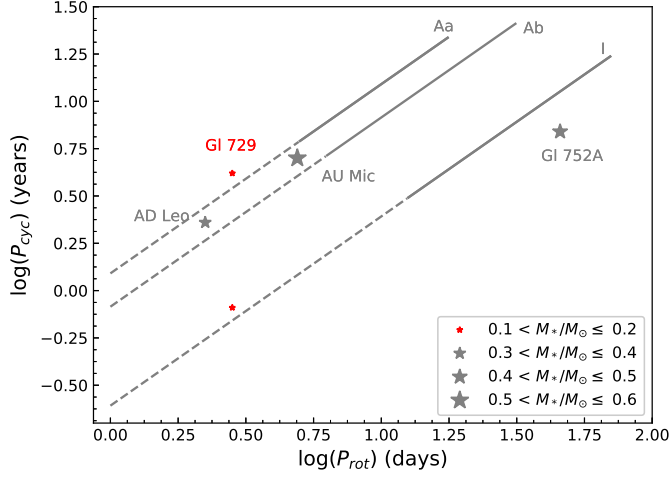


Fig. 12. $\log P_{cyc}$ vs. $\log P_{rot}$. The gray solid lines represent the active (Aa and Ab) and inactive (I) branches reported in Böhm-Vitense (2007), with dashed lines we indicate the extrapolation to lower rotation periods. Gray stars represent the activity cycle periods obtained for the early-M dwarfs GI 752A (Buccino et al. 2011); AD Leo (Buccino et al. 2014) and AU Mic (Ibañez Bustos et al. 2019a). The red stars represent the periods of Gl 729 reported in the present work.

version of Fig. 2 from Böhm-Vitense (2007), and we include one dM and three dMe stars for which we found magnetic activity cycles.

5.3. Wavelet analysis

To explore the strength of the periodic signals we found over time, we performed a wavelet analysis of the seasonal mean S -Index measurements implementing the wavelet analysis described in Torrence & Compo (1998) with the correction developed in Liu et al. (2007). It consists of repeatedly convolving a selected waveform - commonly called the mother wavelet - with the data at each time step, using a range of scales for the waveform. Each scale is associated with a different frequency. The power obtained in each convolution produces a frequency map against the time domain.

In this work we use the Morlet wavelet, which is a sinusoidal signal with a Gaussian amplitude modulation. By sliding it along the time series and changing the scale of the wavelet (that is, its frequency or period), we obtained the wavelet power spectrum (WPS), as the result of the correlation between the wavelet and the data.

Fig. 13 shows the WPS for the time series of Fig. 8. The region delimited by the cross-hatched area is the wavelet region where the edge effects become important, generally defined as “Cone of Influence”. Inside the cone, the power spectrum is shown with a color scale going from the weakest (dark blue) to the strongest (red and brown) signals. We note a significant periodic signal between 3 and 5 years.

We also obtained the global wavelet power spectrum (GWPS), defined as the sum of the WPS over time for each period of the wavelet. We show the GWPS in the right side of the Fig. 13. Following García et al. (2014), we fit the GWPS with a sum of Gaussian curves associated with each peak. The global period extracted corresponds to the highest amplitude peak and its uncertainty is the Half-Width-Half-Maximum (HWHM) of the corresponding Gaussian profile. The horizontal

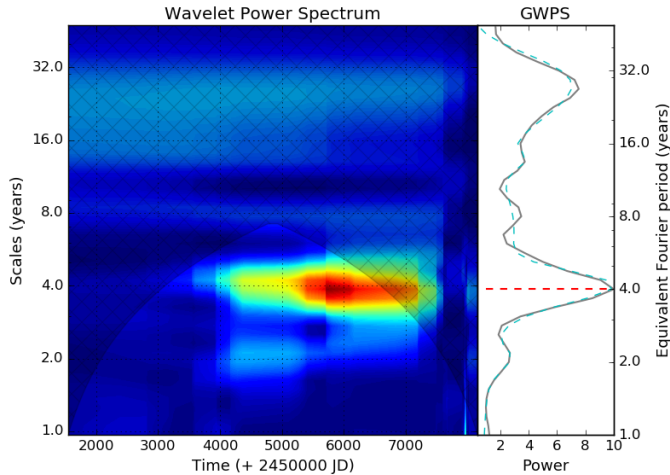


Fig. 13. Contour wavelet plot for Gl 729, calculated using the S time series of Fig. 8. The GWPS is plotted to the right and it is fit by a sum of Gaussians (cyan dashed line). The horizontal red dashed line in the GWPS represents the maximum peak.

red dashed line in the GWPS represents the most significant peak $P_{wave} = 4.1 \pm 0.7$ yr (1497 ± 256 days), in agreement with the 1521 days-period detected with the periodograms above.

Additionally, the wavelet analysis allows us to study the distribution of the cyclic signal throughout the time series. Fig. 13 shows that the 4-year period maintains its strength for most of the observations. However, before $xJD \sim 4000$ days the magnetic activity remains almost constant and the periodic signal is nearly insignificant (see Fig. 13). Around $xJD=4000$ days the level of activity of Gl 729 increases and the cyclic activity becomes more evident, until it reaches a peak after $xJD \sim 6000$, observed in red in the WPS map in Fig. 13. Therefore, we see here the same behaviour we have already seen in Fig. 8.

This phase of flat activity in the range $xJD=1000-4000$ days in Gl 729 resembles the well-known solar Maunder or Dalton Minima, although the sampling in this interval is rather poor and we are probably missing short term variations. Similarly, other solar-type stars also present this behaviour: a broad minimum of activity has also been observed in the K2V star ϵ Eridani (Metcalf et al. 2013) and in the G2V star HD 140538 (Radick et al. 2018). However, this is the first time that it is reported for an M star. Another possible interpretation is that a decadal activity cycle is modulating the 4-year cycle, although further observations of Gl 729 will be needed to confirm this hypothesis.

5.4. Sodium and $H\alpha$ as activity indicators.

The Ca II lines are not the most adequate feature to study chromospheric activity in M stars, which are too faint in that region of the spectrum. To overcome this problem, it is necessary to explore redder activity indicators in these stars. For instance, the $H\alpha$ line has been extensively used as activity indicator (Giampapa & Liebert 1986; Cincunegui et al. 2007b; Robertson et al. 2014), as were other lines, for example the Na I D lines (Díaz et al. 2007a; Gomes da Silva et al. 2012).

The analysis of different chromospheric lines could not only allow us to study magnetic activity at different heights of the atmosphere, but also to understand the energy transport in these regions for different levels of activity in M stars. In particular, atmospheric models of M stars show that the Ca II K line is formed in the lower chromosphere, while the H α line is formed in the upper chromosphere with a different formation regime (e.g. Mauas & Falchi 1994, 1996; Mauas et al. 1997; Fontenla et al. 2016). Walkowicz & Hawley (2009) observed a strong positive correlation between single observations of the Ca II lines and H α in most M3 V active stars. However, this relation is not always valid for multiple observations of an individual active star (Buccino et al. 2014).

The spectra we use in this paper, with the exception of those taken by HIRES and FEROS, cover a wavelength range that allows us to explore different chromospheric features. In particular, we inspect the correlation of simultaneous measurements of the Ca II lines with the H α and Na I D lines obtained for 94 and 87 spectra respectively. To do so, we computed the sodium Na-Index and the H α -Index as defined by Gomes da Silva et al. (2012) and Cincunegui et al. (2007b), respectively. The results are shown in Fig. 14, and in the fifth column of Table 2 we indicate the spectra used in this analysis as “y/y”.

In both cases there is a clear separation in two groups. We separate the points with strong magnetic activity marked with gray circles in Fig. 8, which are indicated with magenta squares. For the remaining points, marked in blue, we found strong correlations in both cases, with Pearson’s coefficients $R = 0.86$ for H α and $R = 0.79$ for Na, as reported by Walkowicz & Hawley (2009) and Díaz et al. (2007a). The variability ($\sigma_X/\langle X \rangle$) of the H α and Na indexes during the cycle (blue points) is around 11 and 12%, respectively, much smaller than the S-Index variability, which is around 27%.

This strong positive correlation seems to change along the activity cycle phase. The H α -index seems to saturate at a value ~ 2.3 at the maximum of the activity cycle (grey points in Fig. 8). Furthermore, it is remarkable that this saturation level is lower than the maximum value reached by the H α -index. A similar behaviour, but with much more spread, is observed in the Na-index.

This saturation could be due to a geometric effect: larger line-fluxes with activity can be due to a larger filling factor of active regions. But the area covered by these active regions increases with height as the magnetic-flux tubes spread out. While the filling factor increases, these tubes get closer, until they eventually cover all the surface higher up in the chromosphere, at the height where H α and the Na D lines are formed, reaching a saturation.

6. Conclusions and summary

New interests in the magnetic activity of M stars have emerged throughout the last decades. On one hand, their strong and moderate flares could severely constrain the habitability of a Terrestrial planet (e.g. Buccino et al. 2007; Vida et al. 2017). On the other hand, due to their internal structures, near and fully-convective stars could be special laboratories to test the dynamo theory.

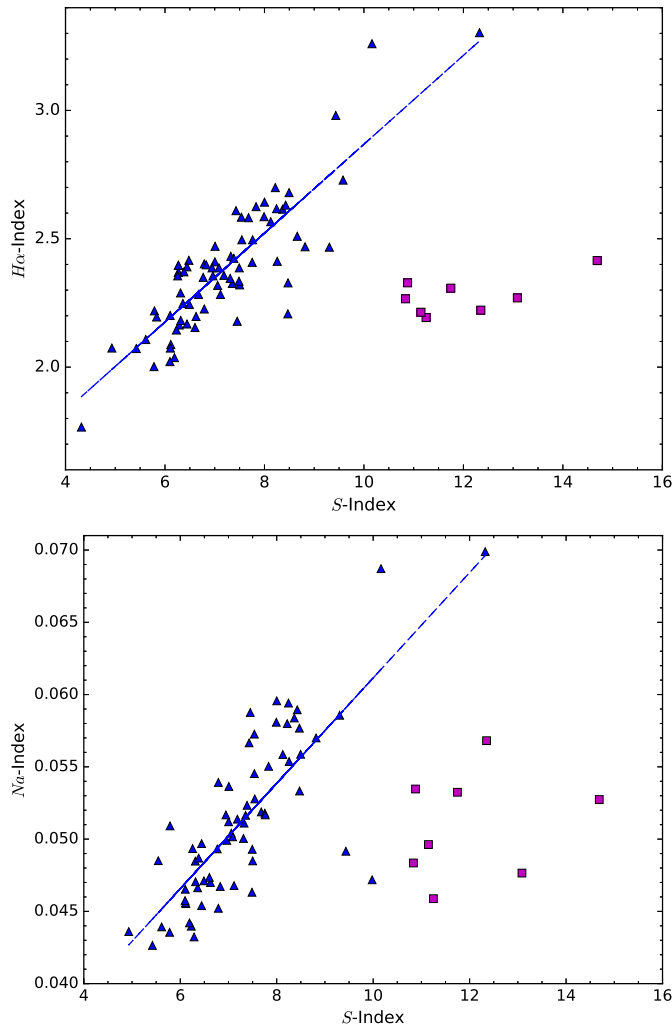


Fig. 14. Simultaneous measurements of the H α (*top*) and the Na I (*bottom*) indexes vs. the Mount Wilson S-Index, for those spectra which include the both features. The magenta squares indicate those points where the level of magnetic activity is increased, some of them associated to flares (gray circles in Fig. 8).

Nevertheless, magnetic activity cycles seem to be present in early, mid and late M dwarfs (e.g., Cincunegui et al. 2007a; Buccino et al. 2011, 2014; Wargelin et al. 2017; Ibañez Bustos et al. 2019a,b; Toledo-Padrón et al. 2019). Furthermore, regardless of whether these stars are fully convective or not, they are placed indistinctly in the two regimes usually observed in the relation of magnetic activity with the stellar parameters (e.g. L_X/L_{bol} vs. P_{rot}/τ in Wright et al. 2011, 2018; $\log R'_{HK}$ vs. P_{rot} in Astudillo-Defru et al. 2017). Thus, the change in the internal structure does not affect the activity-rotation relationship. One of the main conclusion is that stellar rotation could drive the activity in partly and fully convective stars.

In the present work, we contribute to this discussion with an exhaustive study of the fast-rotator dM4 active star, Gl 729. First, we studied its short-term variability due to flares and rotation by a detailed analysis of the long-cadence *Kepler* light curve. We found that this active star presents a flare frequency of 0.5 flares per day with energies between 10^{32} erg and 10^{34} erg, which implies that energy release during these transient events reaches 2 or 4 orders of magnitude more than the

quiescent level. Similar flares were also observed in other M stars (e.g. Hawley et al. 2014; Günther et al. 2020). After discarding the observations associated to flares in the *Kepler* light curve, we obtained a double peaked harmonic curve associated to a rotation period of 2.848 days.

Long-term activity of M stars has been scarcely explored in comparison to solar-type stars. In this work, we derived the Mount Wilson S index using CASLEO, HARPS, FEROS, UVES, XSHOOTER and HIRES spectra. For the whole time series covering 21 years (1998-2019), we detected two significant periods of ~ 4.2 yr and ~ 0.8 yr with four different tools. From our wavelet analysis in Fig. 13 we can determine the distribution of the cyclic signal. We suspect that the 4.2-period is modulated by a decadal activity cycle presenting a minimum in the time range $xJD=1000-4000$ days. Although this behaviour has been observed in several solar-type stars (Metcalf et al. 2013; Radick et al. 2018), it has never been reported in M dwarfs.

We also derived a mean activity level of $\log R'_{HK} = -4.645$ along the time span, in agreement with the value reported in the Astudillo-Defru et al. (2017). Nevertheless, given its rotation period, Gl 729 is placed markedly below the saturation regime in the $\log R'_{HK}$ vs. P_{rot} diagram (see Fig. 10), probably indicating that its activity could be driven by a type of dynamo different than other stars in the graph.

In order to explore the nature of the mechanisms responsible for the cyclical long-term activity detected in Gl 729, we analyzed its surface differential rotation, which is a necessary ingredient for the $\alpha\Omega$ dynamo operation (Charbonneau 2010), whereas it seems not to be determinant in the turbulent α^2 dynamos (e.g. Durney et al. 1993; Chabrier & Küker 2006). To do so, we studied the *Kepler* light-curve with the spot model described in §4.2. In this analysis, we identify two active longitudes and we note some hint for an oscillation in the longitude of the dominant center of activity. However, the amplitude of such a migration, which is of the order of about 50° , is comparable with the longitude resolution achieved by our spot modelling and it is, therefore, no evidence of surface differential rotation. Thus, the activity cycle of Gl 729 could be driven by a turbulent α^2 dynamo.

Cole et al. (2016) studied the oscillatory α^2 dynamo for a one-dimensional mean-field dynamo model. They concluded that long activity cycles can be driven by an α^2 dynamo under certain conditions, if the turbulent diffusivity profile is fairly concentrated toward the equator.

Furthermore the two activity cycles detected in Gl 729, within the statistical error, belong to the active and inactive branch in the $P_{cyc} - P_{rot}$ diagram in Böhm-Vitense (2007). Although this diagram is mainly composed by FGK stars whose activity cycles are probably well reproduced by a solar-type dynamo (e.g. Buccino et al. 2020), it seems that this bimodal distribution in $P_{cyc} - P_{rot}$ could be extended to all cyclic stars, independently of the underlying type of dynamo (see Fig. 12).

All these facts make Gl 729 an ideal target to explore with dynamo models, as it shows signs of long-term cyclic magnetic activity, without evidences of surface differential rotation, which is compatible with a non-solar type dynamo.

References

- Aigrain, S., Parviainen, H., & Pope, B. J. S. 2016, *MNRAS*, 459, 2408
- Andersen, J. M. & Korhonen, H. 2015, *MNRAS*, 448, 3053
- Anglada-Escudé, G., Amado, P. J., Barnes, J., et al. 2016, *Nature*, 536, 437
- Astudillo-Defru, N., Delfosse, X., Bonfils, X., et al. 2017, *A&A*, 600, A13
- Baliunas, S. L., Donahue, R. A., Soon, W. H., et al. 1995, *ApJ*, 438, 269
- Böhm-Vitense, E. 2007, *ApJ*, 657, 486
- Boisse, I., Bonfils, X., & Santos, N. C. 2012, *A&A*, 545, A109
- Bonfils, X., Delfosse, X., Udry, S., et al. 2013, *A&A*, 549, A109
- Bonomo, A. S. & Lanza, A. F. 2012, *A&A*, 547, A37
- Borucki, W. J., Koch, D., Basri, G., et al. 2010, *Science*, 327, 977
- Brandenburg, A., Saar, S. H., & Turpin, C. R. 1998, *ApJ*, 498, L51
- Buccino, A. P., Díaz, R. F., Luoni, M. L., Abrevaya, X. C., & Mauas, P. J. D. 2011, *AJ*, 141, 34
- Buccino, A. P., Lemarchand, G. A., & Mauas, P. J. D. 2007, *Icarus*, 192, 582
- Buccino, A. P., Petrucci, R., Jofré, E., & Mauas, P. J. D. 2014, *ApJ*, 781, L9
- Buccino, A. P., Sraibman, L., Olivar, P. M., & Minotti, F. O. 2020, *MNRAS*, 497, 3968
- Chabrier, G. & Baraffe, I. 1997, *A&A*, 327, 1039
- Chabrier, G. & Küker, M. 2006, *A&A*, 446, 1027
- Charbonneau, P. 2010, *Living Reviews in Solar Physics*, 7, 3
- Charbonneau, P. & MacGregor, K. B. 1997, *ApJ*, 486, 502
- Cincunegui, C., Díaz, R. F., & Mauas, P. J. D. 2007a, *A&A*, 461, 1107
- Cincunegui, C., Díaz, R. F., & Mauas, P. J. D. 2007b, *A&A*, 469, 309
- Cincunegui, C. & Mauas, P. J. D. 2004, *A&A*, 414, 699
- Claret, A. & Bloemen, S. 2011, *A&A*, 529, A75
- Cole, E., Brandenburg, A., Käpylä, P. J., & Käpylä, M. J. 2016, *A&A*, 593, A134
- Davenport, J. R. A., Kipping, D. M., Sasselov, D., Matthews, J. M., & Cameron, C. 2016, *ApJ*, 829, L31
- Desort, M., Lagrange, A. M., Galland, F., Udry, S., & Mayor, M. 2007, *A&A*, 473, 983
- Díaz, R. F., Cincunegui, C., & Mauas, P. J. D. 2007a, *MNRAS*, 378, 1007
- Díaz, R. F., Delfosse, X., Hobson, M. J., et al. 2019, *A&A*, 625, A17
- Díaz, R. F., González, J. F., Cincunegui, C., & Mauas, P. J. D. 2007b, *A&A*, 474, 345
- Díaz, R. F., Ségransan, D., Udry, S., et al. 2016, *A&A*, 585, A134
- Díez Alonso, E., Caballero, J. A., Montes, D., et al. 2019, *A&A*, 621, A126
- Dikpati, M., Gilman, P. A., & MacGregor, K. B. 2005, *ApJ*, 631, 647
- Dressing, C. D. & Charbonneau, D. 2015, *ApJ*, 807, 45
- Duncan, D. K., Vaughan, A. H., Wilson, O. C., et al. 1991, *ApJS*, 76, 383
- Durney, B. R., De Young, D. S., & Roxburgh, I. W. 1993, *Sol. Phys.*, 145, 207
- Engle, S. G. & Guinan, E. F. 2011, in *Astronomical Society of the Pacific Conference Series*, Vol. 451, 9th Pacific Rim Conference on Stellar Astrophysics, ed. S. Qain, K. Leung, L. Zhu, & S. Kwok, 285
- Engle, S. G. & Guinan, E. F. 2018, *Research Notes of the American Astronomical Society*, 2, 34
- Falchi, A., Tozzi, G. P., Falciani, F., & Smaldone, L. A. 1990, *Astrophysical Letters and Communications*, 28, 15
- Fontenla, J. M., Linsky, J. L., Witbrod, J., et al. 2016, *ApJ*, 830, 154
- Gagné, J., Mamajek, E. E., Malo, L., et al. 2018, *ApJ*, 856, 23
- Gaidos, E., Mann, A. W., Lépine, S., et al. 2014, *MNRAS*, 443, 2561
- García, R. A., Ceillier, T., Salabert, D., et al. 2014, *A&A*, 572, A34
- Giampapa, M. S. & Liebert, J. 1986, *ApJ*, 305, 784
- Gizis, J. E., Paudel, R. R., Mullan, D., et al. 2017, *ApJ*, 845, 33
- Gomes da Silva, J., Santos, N. C., Bonfils, X., et al. 2012, *A&A*, 541, A9

- Günther, M. N., Zhan, Z., Seager, S., et al. 2019, arXiv e-prints [arXiv:1901.00443]
- Günther, M. N., Zhan, Z., Seager, S., et al. 2020, *AJ*, 159, 60
- Hawley, S. L., Davenport, J. R. A., Kowalski, A. F., et al. 2014, *ApJ*, 797, 121
- Hawley, S. L., Gizis, J. E., & Reid, I. N. 1996, *AJ*, 112, 2799
- Haywood, R. D., Collier Cameron, A., Queloz, D., et al. 2014, *MNRAS*, 443, 2517
- Ibañez Bustos, R. V., Buccino, A. P., Flores, M., et al. 2019a, *MNRAS*, 483, 1159
- Ibañez Bustos, R. V., Buccino, A. P., Flores, M., & Mauas, P. J. D. 2019b, *A&A*, 628, L1
- Jenkins, J. S., Jones, H. R. A., Pavlenko, Y., et al. 2008, *A&A*, 485, 571
- Johns-Krull, C. M. & Valenti, J. A. 1996, *ApJ*, 459, L95
- Kiraga, M. & Stepień, K. 2007, *Acta Astron.*, 57, 149
- Lamm, M. H., Bailer-Jones, C. A. L., Mundt, R., Herbst, W., & Scholz, A. 2004, *A&A*, 417, 557
- Lanza, A. F. 2016, *Imaging Surface Spots from Space-Borne Photometry*, ed. J.-P. Rozelot & C. Neiner, Vol. 914, 43
- Lanza, A. F., Bonomo, A. S., & Rodonò, M. 2007, *A&A*, 464, 741
- Lanza, A. F., Catalano, S., Cutispoto, G., Pagano, I., & Rodono, M. 1998, *A&A*, 332, 541
- Liu, Y., San Liang, X., & Weisberg, R. H. 2007, *Journal of Atmospheric and Oceanic Technology*, 24, 2093
- Lovis, C., Dumusque, X., Santos, N. C., et al. 2011, ArXiv e-prints [arXiv:1107.5325]
- Malo, L., Artigau, É., Doyon, R., et al. 2014, *ApJ*, 788, 81
- Mauas, P. J. D. & Falchi, A. 1994, *A&A*, 281, 129
- Mauas, P. J. D. & Falchi, A. 1996, *A&A*, 310, 245
- Mauas, P. J. D., Falchi, A., Pasquini, L., & Pallavicini, R. 1997, *A&A*, 326, 249
- McQuillan, A., Aigrain, S., & Mazeh, T. 2013, *MNRAS*, 432, 1203
- Metcalfe, T. S., Buccino, A. P., Brown, B. P., et al. 2013, *ApJ*, 763, L26
- Morris, B. M., Bobra, M. G., Agol, E., Lee, Y. J., & Hawley, S. L. 2020, *MNRAS*, 493, 5489
- Mortier, A., Faria, J. P., Correia, C. M., Santerne, A., & Santos, N. C. 2015, *A&A*, 573, A101
- Muirhead, P. S., Johnson, J. A., Apps, K., et al. 2012, *ApJ*, 747, 144
- Newton, E. R., Irwin, J., Charbonneau, D., et al. 2017, *ApJ*, 834, 85
- Radick, R. R., Lockwood, G. W., Henry, G. W., Hall, J. C., & Pevtsov, A. A. 2018, *ApJ*, 855, 75
- Reiners, A., Joshi, N., & Goldman, B. 2012, *AJ*, 143, 93
- Reiners, A., Zechmeister, M., Caballero, J. A., et al. 2018, *A&A*, 612, A49
- Ribas, I., Tuomi, M., Reiners, A., et al. 2018, *Nature*, 563, 365
- Roberts, D. H., Lehar, J., & Dreher, J. W. 1987, *AJ*, 93, 968
- Robertson, P. & Mahadevan, S. 2014, *ApJ*, 793, L24
- Robertson, P., Mahadevan, S., Endl, M., & Roy, A. 2014, *Science*, 345, 440
- Rodríguez Martínez, R., Lopez, L. A., Shappee, B. J., et al. 2020, *ApJ*, 892, 144
- Saar, S. H. & Brandenburg, A. 1999, *ApJ*, 524, 295
- Suárez Mascareño, A., Rebolo, R., & González Hernández, J. I. 2016, *A&A*, 595, A12
- Toledo-Padrón, B., González Hernández, J. I., Rodríguez-López, C., et al. 2019, *MNRAS*, 488, 5145
- Torrence, C. & Compo, G. P. 1998, *Bulletin of the American Meteorological Society*, 79, 61
- Tsikoudi, V. & Kellett, B. J. 1997, *MNRAS*, 285, 759
- Vida, K., Kóvári, Z., Pál, A., Oláh, K., & Kriskovics, L. 2017, *ApJ*, 841, 124
- Vida, K. & Roettenbacher, R. M. 2018, *A&A*, 616, A163
- Walkowicz, L. M. & Hawley, S. L. 2009, *AJ*, 137, 3297
- Wargelin, B. J., Kashyap, V. L., Drake, J. J., García-Alvarez, D., & Ratzlaff, P. W. 2008, *ApJ*, 676, 610
- Wargelin, B. J., Saar, S. H., Pojmański, G., Drake, J. J., & Kashyap, V. L. 2017, *MNRAS*, 464, 3281
- West, A. A., Hawley, S. L., Walkowicz, L. M., et al. 2004, *AJ*, 128, 426
- West, A. A., Morgan, D. P., Bochanski, J. J., et al. 2011, *AJ*, 141, 97
- Winters, J. G., Medina, A. A., Irwin, J. M., et al. 2019, *AJ*, 158, 152

Wright, N. J. & Drake, J. J. 2016, *Nature*, 535, 526

Wright, N. J., Drake, J. J., Mamajek, E. E., & Henry, G. W. 2011, *ApJ*, 743, 48

Wright, N. J., Newton, E. R., Williams, P. K. G., Drake, J. J., & Yadav, R. K. 2018, *MNRAS*, 479, 2351

Yadav, R. K., Christensen, U. R., Wolk, S. J., & Poppenhaeger, K. 2016, *ApJ*, 833, L28

Zechmeister, M. & Kürster, M. 2009, *A&A*, 496, 577

Table 2. Log of the observations. Col. 1: Spectrograph name; Col. 2: $xJD = JD - 2\,450\,000$, where JD is the Julian date; Col. 3: mean Mount Wilson S -Index; Col. 4: exposure time in seconds; Col. 5: spectrum used in the analysis of section §4 (“y”) or not (“n”), those with “**” are the ones not used in the study, due to the presence of flares; Col. 6: CASLEO label corresponding to a date of each observing run (MMYY); Col. 7: ID programs of the Gl 729 public observations.

Spectrograph	xJD	$\langle S \rangle$	Exp. Time (s)	H_{α}/NaI	ID (only REOSC)	Program ID
REOSC	3545.000000	6.789795e+00	8400	y / y	0605c	
	3926.000000	9.304848e+00	5400	y / y	0706a	
	3955.000000	7.451568e+00	7200	y / y	0806a	
	4165.000000	7.487149e+00	5400	y / y	0307c	
	4281.000000	4.319932e+00	7200	y / n	0607a	
	4367.000000	5.787213e+00	10800	y / y	0907a	
	4730.000000	1.124911e+01	10800	n / n **	0908b	
	4988.000000	1.235089e+01	10800	y / y	0609a	
	5106.000000	1.087805e+01	10800	y / y	1009a	
	5263.000000	1.083528e+01	7200	y / y	0310c	
	5358.000000	8.470264e+00	10800	y / y	0610c	
	5731.000000	6.674119e+00	10800	y / n	0611b	
	5819.000000	9.433980e+00	7200	y / y	0911a	
	6089.000000	1.308467e+01	5400	y / y	0612c	
	6172.000000	1.174740e+01	7200	y / y	0912b	
	6434.000000	1.468871e+01	5400	n / n **	0513a	
	6833.000000	8.659113e+00	5400	y / n	0614b	
	8273.000000	1.114678e+01	7200	y / y	0618a	
8653.000000	9.978682e+00	6000	y / y	0619d		
HARPS	3574.136719	6.789795e+00	900	y / y		072.C-0488(E)
	3607.078125	7.501529e+00	900	y / y		
	7492.320312	7.002447e+00	900	y / y		
	7492.328125	6.360152e+00	900	y / y		
	7493.335938	7.536248e+00	900	n / y		
	7590.027344	6.963389e+00	900	y / y		
	7590.039062	6.768096e+00	900	y / y		
	7593.023438	7.353976e+00	900	y / y		
	7593.035156	7.058867e+00	900	y / y		
	7595.117188	8.495354e+00	1200	y / y		
	7598.207031	7.544929e+00	900	y / y		
	7599.027344	8.256663e+00	900	y / y		
	7599.035156	8.816503e+00	900	y / y		
7600.050781	7.679464e+00	900	y / y			

Table 2. continued.

Spectrograph	xJD	$\langle S \rangle$	Exp. Time (s)	H_{α}/NaI	ID (only REOSC)	Program ID
	7600.062500	6.828854e+00	900	y / y		
	7603.136719	7.115284e+00	900	y / y		
	7603.148438	6.286373e+00	900	y / y		
	7666.992188	8.365159e+00	900	y / y		
	7667.003906	8.243643e+00	900	y / y		
	7667.980469	6.312413e+00	900	y / y		
	7667.992188	7.991933e+00	900	y / y		
	7671.023438	6.624882e+00	900	y / y		
	7904.171875	6.255995e+00	900	y / y		
	7904.183594	6.442607e+00	900	y / y		
	7905.171875	5.422745e+00	900	y / y		
	7905.183594	5.613698e+00	900	y / y		
	7907.125000	8.217604e+00	900	y / y		
	7907.136719	7.831357e+00	900	y / y		
	7918.199219	8.473655e+00	900	y / y		
	7934.160156	7.006788e+00	900	y / y		
	7936.128906	7.427752e+00	900	y / y		
	7937.148438	7.536248e+00	900	y / y		
	7942.093750	6.381851e+00	900	y / y		
	7943.082031	5.544260e+00	900	n / y		
	7944.066406	8.000612e+00	900	y / y		
	7945.109375	6.442607e+00	900	y / y		
	7946.238281	7.323596e+00	900	y / y		
	7953.214844	7.492851e+00	900	y / y		
	7954.136719	1.232309e+01	900	y / y		
	7961.140625	6.117120e+00	900	y / y		
	7962.132812	8.425916e+00	900	y / y		
	7964.144531	6.946029e+00	900	y / y		
	7972.152344	6.316752e+00	900	y / y		
	7974.152344	6.490346e+00	900	y / y		
	7979.214844	8.126467e+00	900	y / y		099.C-0880(A)
	7985.027344	7.753242e+00	900	y / y		
	7986.039062	7.384354e+00	900	y / y		
	7987.050781	6.603183e+00	900	y / y		
	7990.011719	7.761920e+00	900	y / y		
	7992.027344	5.778612e+00	900	y / y		
	7993.011719	6.229956e+00	900	y / y		

Table 2. continued.

Spectrograph	xJD	$\langle S \rangle$	Exp. Time (s)	H_{α}/NaI	ID (only REOSC)	Program ID
	7994.000000	7.310576e+00	900	y / y		
	7995.003906	9.580315e+00	900	y / n		
	7996.007812	1.016185e+01	900	y / y		
	7998.039062	6.108440e+00	900	y / y		
	8001.042969	7.184721e+00	900	y / y		
	8002.031250	7.084904e+00	900	y / y		
	8018.035156	6.190897e+00	900	y / y		
	8019.003906	6.104101e+00	900	y / y		
	8024.089844	6.099760e+00	900	y / y		
FEROS	4166.343750	7.695313e+00	454	n / n		078.A-9058(A)
	5716.335938	6.269531e+00	230	y / n		
UVES	5716.335938	6.269531e+00	230	y / n		087.D-0069(A)
	5716.339844	6.480469e+00	230	y / n		
	7220.070312	5.832031e+00	500	y / n		095.D-0685(A)
XSHOOTER	7185.191406	4.931776e+00	120	y / y		
	7185.195312	4.783937e+00	120	n / n		095.D-0949(A)
	1050.335938	4.758584e+00	400	n / n		U05H
	1051.359375	4.904892e+00	600	n / n		
	1312.566406	4.888838e+00	450	n / n		N22H
	1367.378906	4.686143e+00	400	n / n		N20H
	1703.480469	4.811812e+00	500	n / n		N31H
	2390.609375	7.101417e+00	480	n / n		N11H
HIRES	2803.515625	4.032948e+00	480	n / n		U16H
	2834.394531	4.627389e+00	600	n / n		N15H
	3153.507812	4.281481e+00	480	n / n		U10H
	3239.343750	5.095374e+00	500	n / n		U09H
	3548.460938	6.789794e+00	500	n / n		N59H
	3934.335938	6.148695e+00	500	n / n		N054Hr
	5409.390625	6.813473e+00	600	n / n		H222Hr